GEOPHYSICS, VOL. 82, NO. 4 (JULY-AUGUST 2017); P. S315–S325, 19 FIGS.
10.1190/GEO2016-0564.1

Check for updates

Downloaded 06/21/17 to 138.67.129.34. Redistribution subject to SEG license or copyright; see Terms of Use at http://library.seg.org/

Elastic least-squares reverse time migration

Yuting Duan[1], Antoine Guitton[1], and Paul Sava[1]

ABSTRACT

Least-squares migration can produce images with improved resolution and reduced migration artifacts, compared with conventional imaging. We have developed a method for elastic least-squares reverse time migration (LSRTM) based on a new perturbation imaging condition that yields scalar images of squared P- and S-velocity perturbations. These perturbation images do not suffer from polarity reversals that are common for more conventional elastic imaging methods. We use 2D synthetic and field-data examples to demonstrate the proposed LSRTM algorithm using the perturbation imaging condition. Our results show that elastic LSRTM improves the energy focusing and illumination of the elastic images and it attenuates artifacts resulting, for instance, from sparseness in the wavefield sampling and crosstalk of the P- and S-modes. Compared with RTM images, the LSRTM images provide more accurate relative amplitude information that is useful for reservoir characterization.

INTRODUCTION

Seismic migration is a technique for obtaining structural images of the subsurface from recorded seismic data. Starting from a linearized forward operator that is based on assumptions about the wave equation and model parameters, seismic migration can be formulated as the adjoint operator that maps seismic data to a subsurface image (Claerbout, 1992). Migrated images not only can show geologic structures but they also can provide information about material properties, such as reflectivity, which is important for reservoir characterization. In practice, however, migration images often contain various undesirable artifacts, for example, the artifacts caused by limited bandwidth and acquisition coverage. Also, migration images are usually computed under assumptions about wave propagation in the subsurface, e.g., that the earth is isotropic and acoustic; these assumptions do not fully represent the real elastic earth. Taken together, these limitations and assumptions result in artifacts.

Advances in seismic acquisition and ongoing improvements in computational capability make imaging using elastic waves increasingly feasible (Sun and McMechan, 1986; Hokstad et al., 1998; Sun et al., 2006; Denli and Huang, 2008; Yan and Sava, 2008; Artman et al., 2009; Wu and Yan, 2010; Du et al., 2012b; Duan and Sava, 2015; Rocha et al., 2016). Compared with acoustic images, elastic images can provide more information about the subsurface, e.g., fracture distributions and elastic properties. However, elastic migration suffers from issues that negatively affect the quality of the images. Because it is, in general, difficult to separate all arrivals by wave mode in recorded data, nonphysical modes lead to artifacts (i.e., crosstalk) in the image (Duan and Sava, 2014).

Least-squares migration (LSM) is an improved imaging algorithm that reduces these migration artifacts and also improves the resolution of migration images. LSM is a linearized waveform inversion that seeks to find the image that best predicts, in a least-squares sense, the recorded seismic data (Schuster et al., 1993; Nemeth et al., 1999; Kuehl and Sacchi, 2002; Kaplan et al., 2010). Schuster et al. (1993) propose LSM for crosswell data, whereas Nemeth et al. (1999) apply this technique to surface data. Their studies show that LSM can significantly improve the spatial resolution of the images and can also reduce migration artifacts arising from limited aperture, coarse sampling, and acquisition gaps.

LSM can be implemented using a Kirchhoff engine (Nemeth et al., 1999; Dai et al., 2011), one-way wave propagator (Kuehl and Sacchi, 2002; Kaplan et al., 2010; Huang and Schuster, 2012), or two-way wave propagator, i.e., least-squares reverse time migration (LSRTM) (Dong et al., 2012; Dai and Schuster, 2013; Hou and Symes, 2015; Wong et al., 2015). For elastic LSM, Stanton and Sacchi (2015) propose elastic LSM using a one-way wave equation, and they compute PP and PS images from 2C elastic data in isotropic media. Although computationally expensive, RTM is advantageous for velocity models with strong lateral variations or with complicated geologic structures that result in wavefield multipathing.

Manuscript received by the Editor 1 November 2016; revised manuscript received 5 February 2017; published online 30 May 2017.
[1]Center for Wave Phenomena, Colorado School of Mines, Golden, Colorado, USA. E-mail: yduan@mines.edu; aguitton@gmail.com; psava@mines.edu.
© 2017 Society of Exploration Geophysicists. All rights reserved.

Downloaded 06/21/17 to 138.67.129.34. Redistribution subject to SEG license or copyright; see Terms of Use at http://library.seg.org/

A key component for elastic LSRTM is the imaging condition, and many different types of imaging conditions have been proposed for elastic media. For example, Yan and Sava (2008) propose a displacement imaging condition that crosscorrelates each component of the source and receiver displacement wavefields. They also propose a potential imaging condition that crosscorrelates P- and S-wave modes derived from the source and receiver wavefields. One issue with this potential imaging condition is that the image components for converted waves change polarity at normal incidence. Therefore, they adopt an additional polarity correction in the angle domain, which is computationally expensive. Duan and Sava (2015) propose a scalar imaging condition for converted waves that produces scalar images without polarity reversal; however, this imaging condition requires knowledge of the geologic dip. Du et al. (2012a) reverse the polarity in source and receiver wavefields based on the directions of the incident and reflected waves. These directions typically are computed using Poynting vectors, which may be inaccurate in complicated models characterized by multipathing (Dickens and Winbow, 2011; Patrikeeva and Sava, 2013).

In this paper, we propose an elastic LSRTM method based on a new perturbation imaging condition, which is derived for squared P and S velocities. Images computed using this new imaging condition can be related to physical subsurface properties, and they do not suffer from polarity changes; they can be stacked over experiments without an additional polarity correction, thus reducing the computational cost of the algorithm. Using 2D synthetic and field-data examples, we demonstrate that we are able to obtain elastic LSRTM images with higher resolution and reduced migration artifacts.

THEORY

LSM aims to find the image that best predicts, in a least-squares sense, the recorded seismic data. For elastic migration, we consider a vector image $\mathbf{m}$, which contains P- and S-wave lithologic information. We treat migration as an adjoint operator $\mathbf{F}^{\mathrm{T}}$ that transforms data $\mathbf{d}$ to image $\mathbf{m}$, and thus the forward process can be expressed as

$$\mathbf{Fm} = \mathbf{d}, \tag{1}$$

where $\mathbf{F}$ is the demigration operator. Data $\mathbf{d}(e, \mathbf{x}, t)$ are a vector, as a function of the experiment index e, spatial location x, and time t.

For LSM, one typically updates the model iteratively by minimizing the objective function:

$$\mathcal{J} = \sum_e \frac{1}{2} \|\mathbf{W}(\mathbf{Fm} - \mathbf{d}_r)\|^2, \tag{2}$$

which evaluates the misfit between the observed data $\mathbf{d}_r$ and predicted data $(\mathbf{Fm})$ for each experiment e. The operator $\mathbf{W}(e, \mathbf{x}, t)$ denotes a data weighting operator, which can be applied for various purposes. For example, Trad et al. (2015) use a matrix $\mathbf{W}$ to eliminate the impact of high-amplitude noise or missing traces on inversion; Wong et al. (2015) use $\mathbf{W}$ to weigh the salt reflection energy down. In this paper, we use the data weighting term to equalize the amplitudes of all arrivals in the recorded data, and thus to obtain balanced updates for all reflectors.

We derive perturbation models using the Born approximation (Hudson and Heritage, 1981; Jaramillo and Bleistein, 1999; Ribodetti et al., 2011). We consider the homogeneous elastic isotropic wave equation:

$$\ddot{\mathbf{u}}_s - \alpha\nabla(\nabla \cdot \mathbf{u}_s) + \beta\nabla \times (\nabla \times \mathbf{u}_s) = \mathbf{d}_s. \tag{3}$$

The background elastic models are assumed to be slowly varying. Vector $\mathbf{u}_s(e, \mathbf{x}, t) = [\mathbf{u}_x \quad \mathbf{u}_y \quad \mathbf{u}_z]^T$ is the source-displacement wavefield, which is a function of experiment e, space x, and time t. The vector $\mathbf{d}_s(e, \mathbf{x}, t)$ is the source function, which we assume to be known. The parameters $\alpha(\mathbf{x}) = (\lambda + 2\mu)/\rho$ and $\beta(\mathbf{x}) = (\mu/\rho)$ are the squared P- and S-wave velocities, respectively; λ and μ are the Lamé parameters, and ρ is the density.

The perturbation $\mathbf{m} = [\delta\alpha \quad \delta\beta]^T$ added to the background model gives the perturbed model $[\alpha + \delta\alpha \quad \beta + \delta\beta]^T$. Under the Born approximation, the total wavefield $\mathbf{u}_s + \delta\mathbf{u}_s$ is computed using the same source term $\mathbf{d}_s$:

$$(\ddot{\mathbf{u}}_s + \delta\ddot{\mathbf{u}}_s) - (\alpha + \delta\alpha)\nabla[\nabla \cdot (\mathbf{u}_s + \delta\mathbf{u}_s)] + (\beta + \delta\beta)\nabla \times [\nabla \times (\mathbf{u}_s + \delta\mathbf{u}_s)] = \mathbf{d}_s, \tag{4}$$

where $\delta\mathbf{u}_s$ is the perturbed wavefield.

By ignoring the high-order terms $\delta\alpha\nabla(\nabla \cdot \delta\mathbf{u}_s)$ and $\delta\beta\nabla \times (\nabla \times \delta\mathbf{u}_s)$, and subtracting equation 3 from equation 4, we obtain a relation for the perturbed wavefield $\delta\mathbf{u}_s$ with respect to the model perturbations in α and β:

$$\delta\ddot{\mathbf{u}}_s - \alpha\nabla(\nabla \cdot \delta\mathbf{u}_s) + \beta\nabla \times (\nabla \times \delta\mathbf{u}_s) = [\nabla(\nabla \cdot \mathbf{u}_s) - \nabla \times (\nabla \times \mathbf{u}_s)] \begin{bmatrix} \delta\alpha \\ \delta\beta \end{bmatrix}. \tag{5}$$

The predicted data are extracted from the perturbed wavefield $\delta\mathbf{u}_s$ at the receiver locations.

We define an operator $\mathbf{Q}$ that, at each time and space position, computes the dot product between vector $[\nabla(\nabla \cdot \mathbf{u}_s) - \nabla \times (\nabla \times \mathbf{u}_s)]^T$ and the image $\mathbf{m}$. Here, the first and second elements of this vector used by operator $\mathbf{Q}$ are the decomposed P- and S-modes of the source wavefield $\mathbf{u}_s$, respectively. The demigration operator in equation 1 thus becomes

$$\mathbf{F} = \mathbf{KPQ}, \tag{6}$$

where $\mathbf{P}$ represents an elastic forward modeling operator that computes the perturbed wavefield $\delta\mathbf{u}_s$ for a source term $\mathbf{Qm}$ and $\mathbf{K}$ is an operator that restricts the perturbed wavefield $\delta\mathbf{u}_s$ to the known receiver positions. Equation 6 maps the image $\mathbf{m}$ to the data $\mathbf{d}_r$, and its adjoint operator,

$$\mathbf{F}^{\mathsf{T}} = \mathbf{Q}^{\mathsf{T}}\mathbf{P}^{\mathsf{T}}\mathbf{K}^{\mathsf{T}}, \tag{7}$$

maps the data $\mathbf{d}_r$ to the image $\mathbf{m}$; the operator $\mathbf{K}^{\mathsf{T}}$ injects the recorded data $\mathbf{d}_r$ into the wavefield, and the adjoint wave-propagation operator $\mathbf{P}^{\mathsf{T}}$ computes the receiver displacement wavefield $\mathbf{u}_r = \mathbf{P}^{\mathsf{T}}\mathbf{K}^{\mathsf{T}}\mathbf{d}_r$. Equation 7 describes a perturbation imaging condition for elastic RTM because the application of the adjoint operator $\mathbf{F}^{\mathsf{T}}$ to the recorded data $\mathbf{d}_r$ yields the images

$$\delta\alpha = \sum_{e,t} \nabla(\nabla \cdot \mathbf{u}_s) \cdot \mathbf{u}_r, \tag{8}$$

$$\delta\beta = \sum_{e,t} -\nabla \times (\nabla \times \mathbf{u}_s) \cdot \mathbf{u}_r, \tag{9}$$

Downloaded 06/21/17 to 138.67.129.34. Redistribution subject to SEG license or copyright; see Terms of Use at http://library.seg.org/

for the α and β models, respectively. From equations 8 and 9, we see that images $\delta\alpha$ and $\delta\beta$ are computed by taking the zero-lag cross-correlation of elements used by operator $\mathbf{Q}$ with the displacement receiver wavefield $\mathbf{u}_r$. These images indicate the model perturbations, instead of the reflection coefficients; therefore, they do not suffer from polarity reversal, which is a common issue for elastic images, whose values are related to angle-dependent reflectivity. Because our inversion algorithm updates $\delta\alpha$ and $\delta\beta$ images simultaneously, we apply a scaling factor ϵ to the image $\delta\beta$ to balance the updates of the two images. For the following synthetic examples, we use $\epsilon = 1$; for the field-data example, we estimate ϵ by comparing the root-mean-square values of gradients in the first iteration of independent inversions for $\delta\alpha$ and $\delta\beta$. We use a conjugate direction solver for inversion (Claerbout, 2014).

EXAMPLES

We show the results of our elastic LSRTM method using three examples. First, we run an inversion with a simple synthetic layered model, and we analyze the relationships of model perturbations and elastic reflections. Second, we test the method using a more complex model. We use the elastic Marmousi model to generate perturbation models, background models, and a 2C data set. Finally, we apply our method to a real 2D ocean bottom cable (OBC) data set and compare the elastic RTM images with the LSRTM images.

Layered model

We use a simple example to demonstrate the algorithms for elastic migration. Each of the α and β models contains one horizontal reflector, but the two reflectors are at different depths, as shown in Figure 1a and 1b. We generate 30 2C shot gathers using a vertical displacement source with a 30 Hz peak frequency Ricker wavelet. Figure 2a–2f shows the x- and z-component snapshots of a wavefield with the source at (0.76, 0.06) km. The P-wave generates reflections at the reflector in the α model, but not at the reflector in the β model. Similarly, the S-wave generates reflections at the reflector in the β model, but not at the reflector in the α model. The x- and z-components of this shot gather after direct wave removal are shown in Figure 3a and 3b, respectively. Note the four strong arrivals, which are, from top to bottom, PP, PS, SP, and SS reflections. Using the perturbation imaging condition (equation 6), we obtain the perturbation images for $\delta\alpha$ and $\delta\beta$ shown in Figure 4a and 4b, respectively. Notice that additional reflectors appear in $\delta\alpha$ and $\delta\beta$ images, and these reflectors are generated by fake modes in the constructed receiver wavefield.

Figure 4c and 4d shows the LSRTM images after 10 iterations. Compared with the RTM images (Figure 4a and 4b), the artifacts in the LSRTM images are attenuated. Moreover, the peak values of the LSRTM images at $x = 0.6$ km are closer to the amplitudes of the true perturbation compared with the values of the RTM images. Therefore, LSRTM improves elastic imaging with true amplitude information and fewer artifacts, such as artifacts caused by the nonphysical modes.

Marmousi model

The Marmousi II model (Martin et al., 2006) is fully elastic, which supports not only P-waves but also S-waves and converted waves. The model simulates hydrocarbon reservoirs that dramatically decrease the value of α but slightly increase the value of β. We smooth the original Marmousi II model horizontally and vertically to obtain the background models for α and β, shown in Figure 5a and 5b, respectively. We add a homogeneous layer at the top of each model. Figure 6a and 6b shows the corresponding true perturbation models for $\delta\alpha$ and $\delta\beta$, respectively, which are inconsistent in reservoir areas; e.g., only the $\delta\alpha$ model shows a reflector with a negative value at (2, 0.4) km. This inconsistency poses a challenge for elastic LSRTM, e.g., if the inversion allows a leakage between model parameters.

We model 40 shots evenly spaced on the surface using a displacement source with a 30 Hz peak frequency Ricker wavelet. The horizontal and vertical components of the source function have the same amplitude to generate strong S-waves. The receiver spread is fixed for all shots and spans from 0 to 3.0 km with 5 m sampling.

The recorded data are modeled according to equation 7. The z-component of one shot gather with the source location at (1.54, 0.013) km is shown in Figure 7a. The arrival with high amplitude is the reflection from the bottom of the homogeneous layer, and its amplitude is much stronger than other arrivals in the recorded data. Thus, this arrival generates strong artifacts in the computed image, and the inversion mostly focuses on generating an image that best

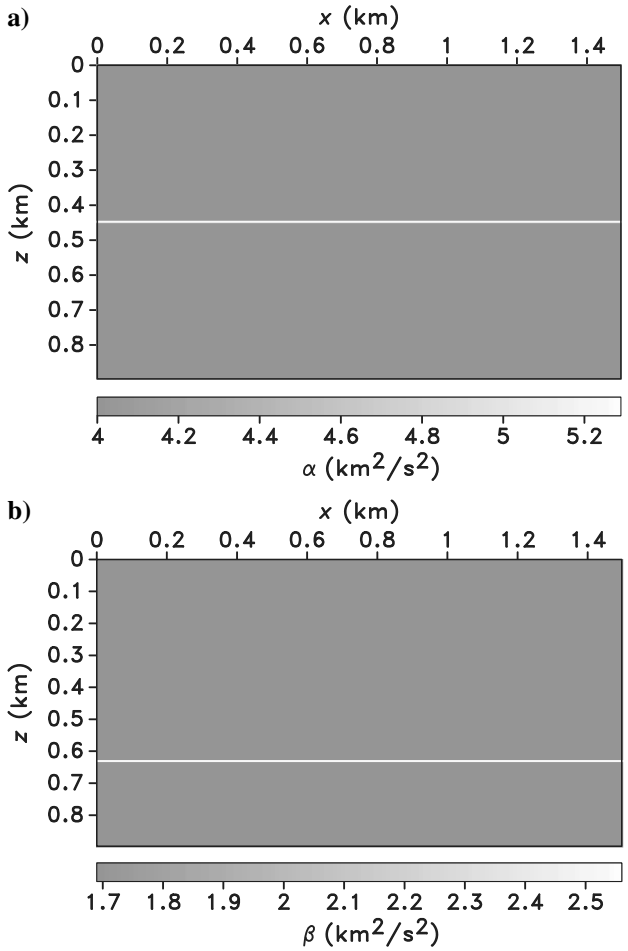


Figure 1. Synthetic layered model example. (a) The α model with a horizontal reflector at $z = 0.45$ km, and (b) β model with a horizontal reflector at $z = 0.62$ km.

matches these strong arrivals, instead of the late arrivals with weaker amplitudes. To obtain a more uniform update using all arrivals, we use the data-weighting term **W**. The data-weighting matrix is the inverse of the envelope of the recorded data, which weights down the strongest arrivals. We also apply a smoothing operator in the data space to the weighting function to avoid discontinuity along the time and space axes. Figure 7b shows the weighting function in the data domain, which we compute from the shot gather (Figure 7a). Figure 8 shows the z-component of the weighted shot gather. Compared with the original recorded data (Figure 7a), the amplitudes of the arrivals in the weighted data (Figure 8) are more balanced.

Figure 9a and 9b shows the RTM images for $\delta\alpha$ and $\delta\beta$, respectively. We observe that the events for the shallow reflectors in both models have stronger amplitudes compared with those of the deeper reflectors, and strong backscattering is present due to the sharp interfaces in the background model. We apply an illumination compensation based on the source wavefield to the RTM images and LSRTM gradients, to balance nonuniform data coverage.

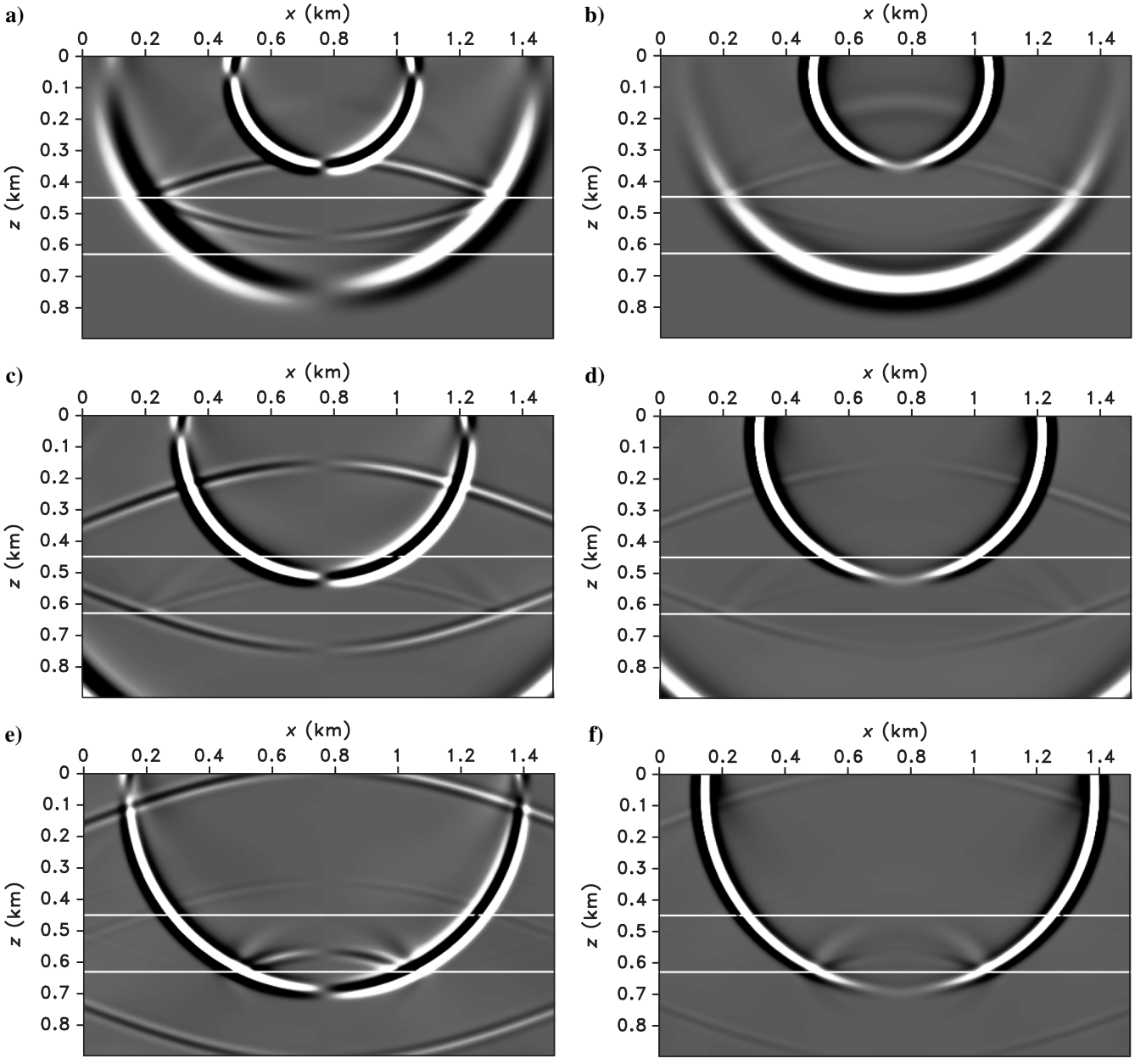


Figure 2. Synthetic layered model example. Snapshots of an elastic wavefield, for a source at coordinates (0.76, 0.06) km: (a) x- and (b) z-components of the wavefield at $t = 0.2$ s; (c) x- and (d) z-components of the wavefield at $t = 0.3$ s; and (e) x- and (f) z-components of the wavefield at $t = 0.4$ s. Two horizontal lines indicate the locations of reflectors in α and β models. The P-waves generate reflections only at the top reflector; and the S-waves generate reflections only at the bottom reflector.

Downloaded 06/21/17 to 138.67.129.34. Redistribution subject to SEG license or copyright; see Terms of Use at http://library.seg.org/

Downloaded 06/21/17 to 138.67.129.34. Redistribution subject to SEG license or copyright; see Terms of Use at http://library.seg.org/

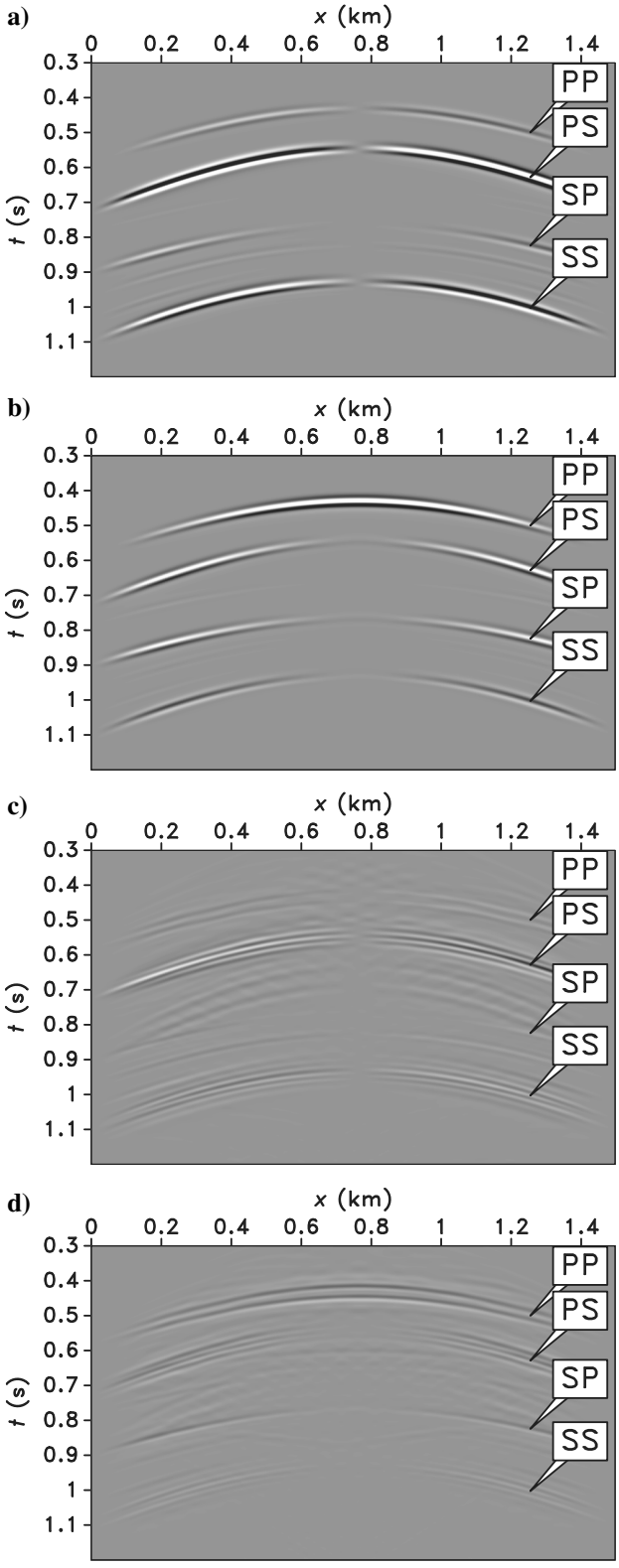


Figure 3. Synthetic layered model example. For the source at (0.76, 0.06) km, (a) x- and (b) z-components of the recorded data; and (c) x- and (d) z-components of the data difference using the inverted model. The direct arrivals are removed in the shot gathers. Note that the predicted data match the recorded data in phase and amplitude.

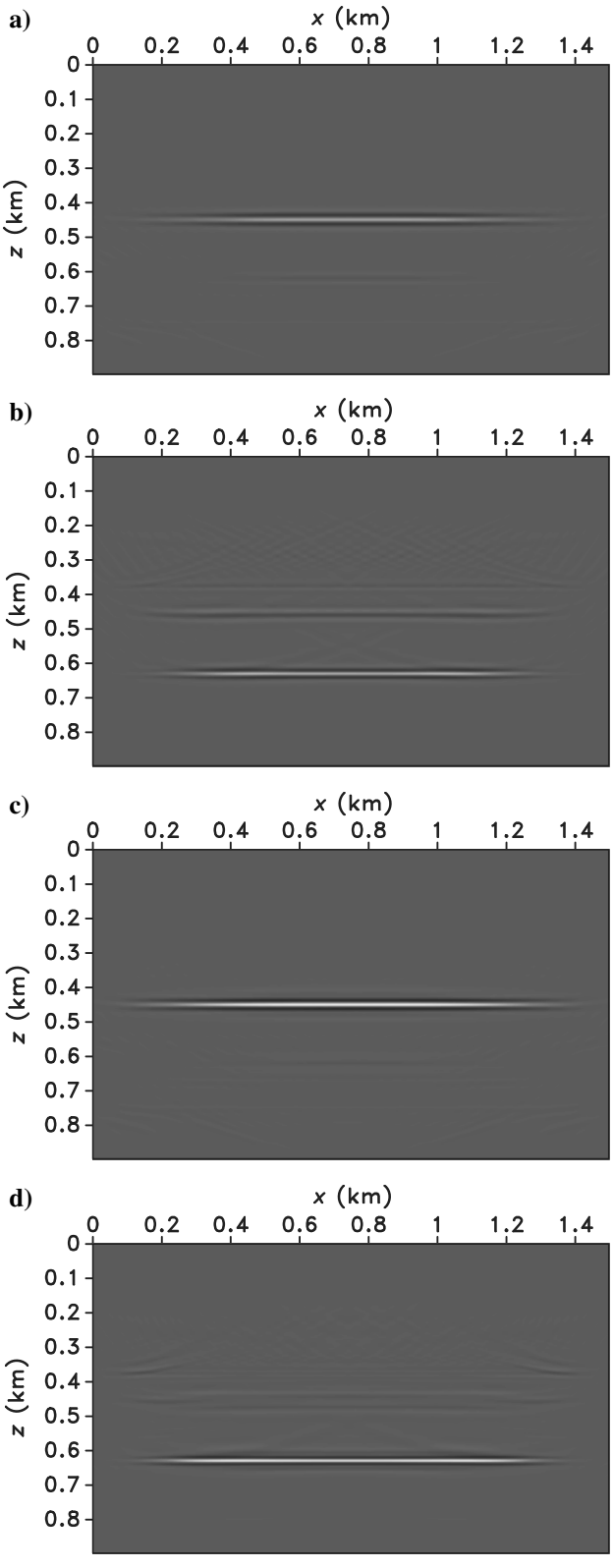


Figure 4. Synthetic layered model example. (a) The $\delta\alpha$ and (b) $\delta\beta$ images after first iteration. In addition to the event at the correct depth, there are two strong horizontal events in the $\delta\beta$ image, which are the crosstalk artifacts. (c) The $\delta\alpha$ and (d) $\delta\beta$ images after 10 iterations. Compared with the $\delta\alpha$ and $\delta\beta$ images after the first iteration, the artifacts have been attenuated.

Downloaded 06/21/17 to 138.67.129.34. Redistribution subject to SEG license or copyright; see Terms of Use at http://library.seg.org/

The LSRTM images after 60 iterations are shown in Figure 10a and 10b. Figure 11a shows the convergence curve. The updated image for $\delta\beta$ has higher resolution than $\delta\alpha$ because, in general, S-waves have shorter wavelengths than P-waves, and we do not consider attenuation in this experiment. The updated images are consistent with the true perturbation images (Figure 6a and 6b). For example, only the $\delta\alpha$ image (Figure 10a) contains the reflector with negative value at (2, 0.4) km, which corresponds to a hydrocarbon reservoir in the true model that only decreases the value of α.

The same weighting functions are applied to the two gathers. Figure 11b shows the z-component of data difference. The amplitudes of all arrivals in the data residual after inversion are small; i.e., for most arrivals, the predicted data match the recorded data in phase and amplitude. Because we use Born data generated using the same wave equation as the recorded data, the amplitudes of the LSRTM images match well the true perturbation models. In practice, with errors in the background models and approximations of the wave equation, we may not obtain true-amplitude LSRTM images; however, the relative amplitudes of the reflectors can still be estimated correctly, which is beneficial for reservoir characterization.

Volve OBC data

We apply our elastic LSRTM method to data from the Volve field, located in the Norwegian North Sea. The Volve field has an average water depth of 90 m, and the field is characterized by a complex subchalk reservoir (Szydlik et al., 2007). We are provided with processed PP and PS data, recorded in an acquisition geometry consisting of 12 parallel receiver lines each with 240 receivers. However, because PP and PS data typically are intended for independent PP and PS migrations, they are not well-suited for our inversion algorithm, which requires full components of displacement data. For our test, we use a 2D line extracted from only the PP data set, which we treat as the vertical component of the displacement vector. We band-pass the data between 0 and 15 Hz to attenuate high-frequency noise and to reduce the computational cost, and we apply a gain in time to compensate for 3D effects. Figure 12a shows one shot gather at $x = 6$ km, with the band-pass filter and 3D compensation applied. The arrivals at 2.5–3.0 s are PP reflections from the chalk layer.

Additional processing is required to condition the data for elastic LSRTM. Because S-waves were purposely attenuated in the provided PP data in preparation for acoustic imaging, we use a data-weighting function (Figure 12b) for elastic imaging to attenuate predicted S-wave arrivals that otherwise would result in a large data misfit. This data-weighting function also incorporates a mask to mute direct arrivals, as well as an additional weight that boosts later arrivals to balance reflector amplitudes in the migration images.

The background α and β models are shown in Figure 13a and 13b, respectively, and they are computed from the provided P- and S-velocity models. We apply additional vertical and horizontal smoothing to the original models, so that the background models

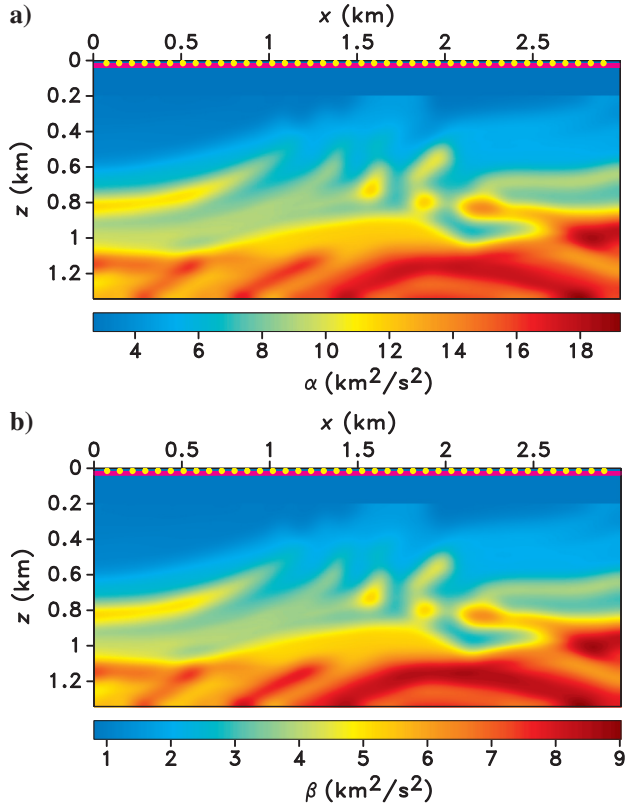


Figure 5. Synthetic Marmousi model example. Background (a) α and (b) β models. The receivers are at depth $z = 0.025$ km, and the sources are at depth $z = 0.013$ km. The top layer is homogeneous for both background models.

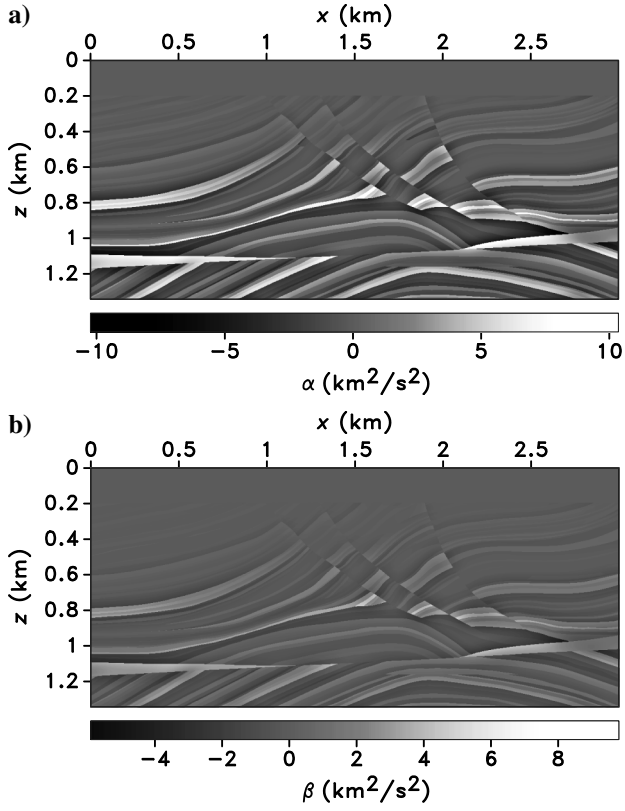


Figure 6. Synthetic Marmousi model example. True (a) $\delta\alpha$ and (b) $\delta\beta$ perturbation models. The perturbation models are not identical; e.g., a reflector with negative value at (2, 0.4) km is present only in the $\delta\alpha$ model.

Downloaded 06/21/17 to 138.67.129.34. Redistribution subject to SEG license or copyright; see Terms of Use at http://library.seg.org/

follow our assumption of homogeneous or slowly varying elastic media. A source wavelet for migration is estimated from the zero-offset data by matching the observed and predicted data using the background models. Using these models and an estimated source wavelet, we compute the RTM images shown in Figure 14a and 14b, in which we observe reflectors, as well as the migration artifacts.

For elastic LSRTM, we invert for $\delta\alpha$ and $\delta\beta$ images simultaneously. The scaling factor ϵ is 0.5, which is applied to $\delta\beta$ image to balance the updates of the two images. Figure 15a and 15b shows the LSRTM images after 12 iterations, at which point the convergence curve (Figure 16) becomes flat. Compared with the RTM images, the LSRTM images have higher resolution and better balanced reflector amplitudes. In addition, shallow reflectors in the LSRTM image for $\delta\beta$ (Figure 15b) are much more continuous and have larger lateral extent along the x-direction, for example, at $z = 1.0$ and 1.5 km. After the inversion converges, some reflectors of less than $z = 3.5$ km in the α image are eliminated; however, they appear as strong and continuous reflectors in the $\delta\beta$ image. Figure 17a and 17b shows the observed and predicted shot gathers at $x = 6$ km, respectively, and Figure 17c shows the data difference plotted on the same scale. The predicted data accurately reproduce the dominant reflection energy seen in the observed data, and the remaining residual in the data difference contains mostly noise and some weaker reflection events. Some of these reflections with steep slopes are predicted S-waves that are missing in the observed data. Other weak reflections in the data residual may be due to anisotropy of the field, which is not considered in our current implementation of the algorithm.

To evaluate the reflectors in the $\delta\alpha$ and $\delta\beta$ images, we generate the predicted shot gathers using $\delta\alpha$ and $\delta\beta$ LSRTM images individually. By comparing these shot gathers with the observed data (Figure 17a), we notice that the inverted $\delta\alpha$ image predicts most of the arrivals in the observation with correct amplitudes (Figure 18a). The reflections predicted by the $\delta\beta$ image (Figure 18b) are relatively weaker than those predicted by the $\delta\alpha$ image.

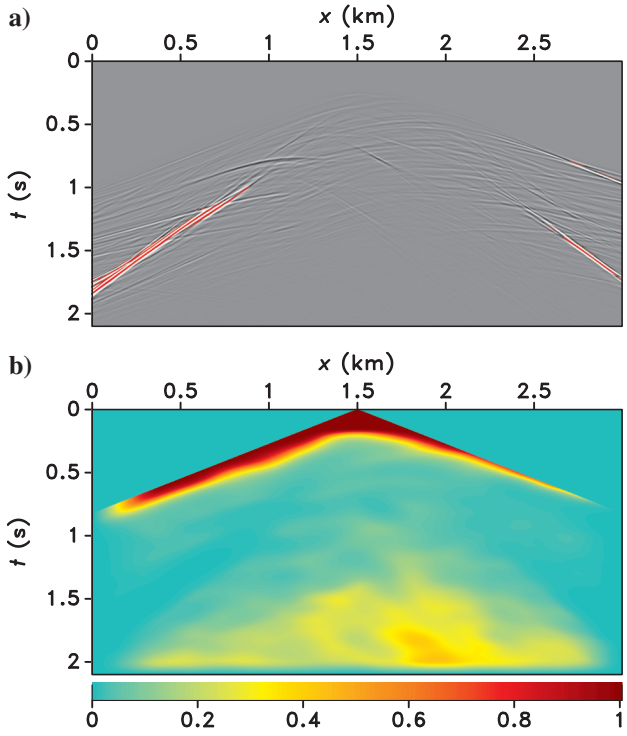


Figure 7. Synthetic Marmousi model example. For the source location at (1.54, 0.013) km, (a) z-component of one shot gather. The highlighted arrival is the reflection from the bottom of the homogeneous layer, and its amplitude is much stronger than other arrivals in the recorded data. (b) The data weighting function generated from the recorded data. The same weighting function is applied to the horizontal and vertical components of the shot gather.

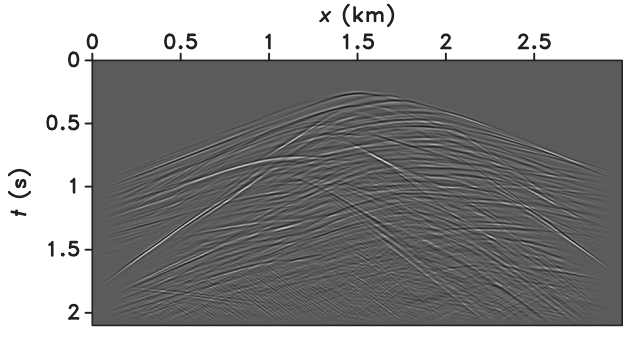


Figure 8. Synthetic Marmousi model example. For the source location at (1.54, 0.013) km, z-components of the weighted shot gather. Note that the amplitudes of all arrivals are more balanced compared with Figure 7a.

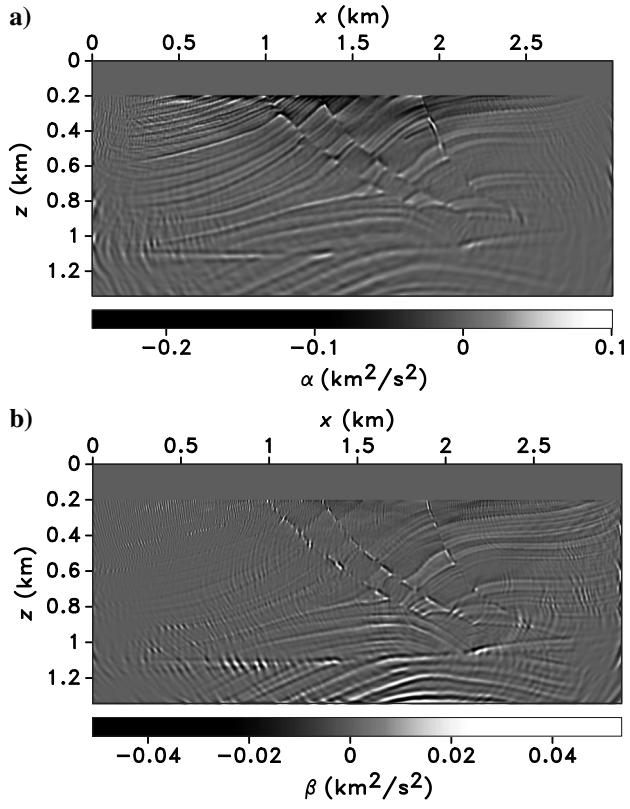


Figure 9. Synthetic Marmousi model example. (a) The $\delta\alpha$ and (b) $\delta\beta$ RTM images with illumination compensation based on the source wavefield.

Downloaded 06/21/17 to 138.67.129.34. Redistribution subject to SEG license or copyright; see Terms of Use at http://library.seg.org/

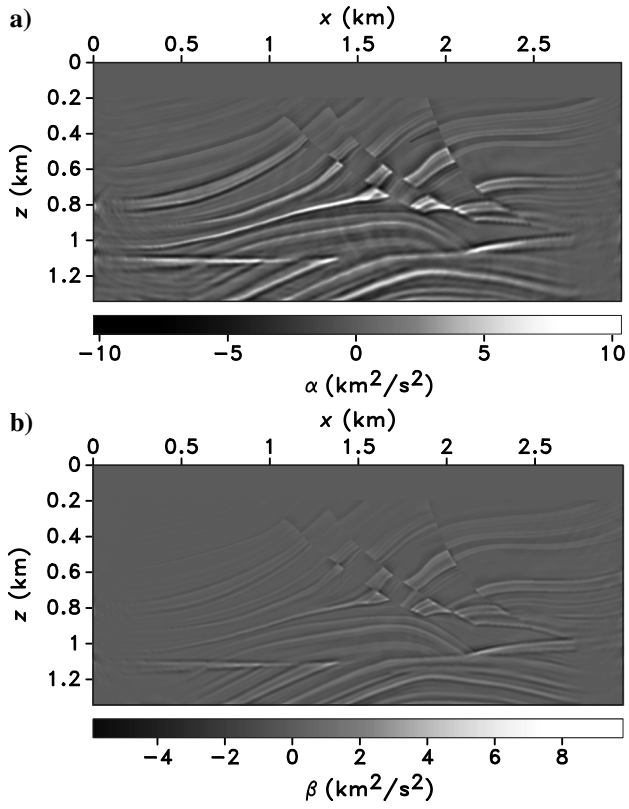


Figure 10. Synthetic Marmousi model example. Updated (a) $\delta\alpha$ and (b) $\delta\beta$ images after 60 iterations. Note that the reservoir near coordinates (2.0, 0.4) km is correctly recovered in the updated $\delta\alpha$ image, without any leakage in the updated $\delta\beta$ image.

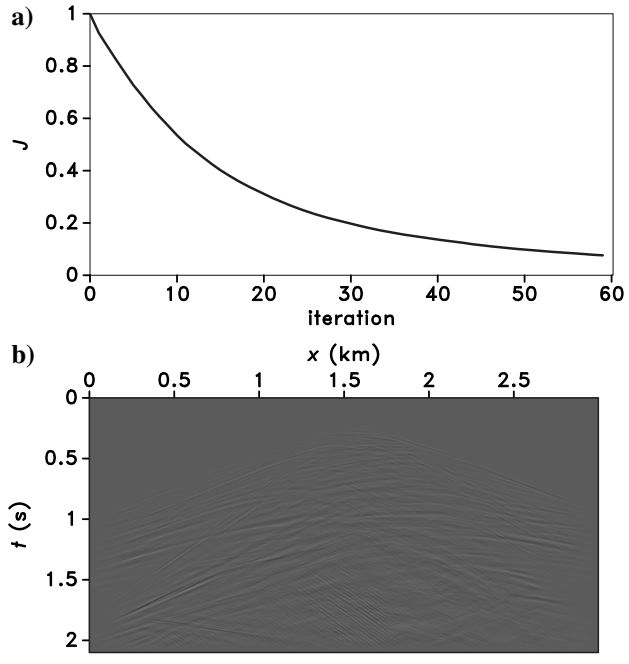


Figure 11. Synthetic Marmousi model example. (a) The convergence curve. (b) The z-component of the data difference using the updated models (Figure 10a and 10b).

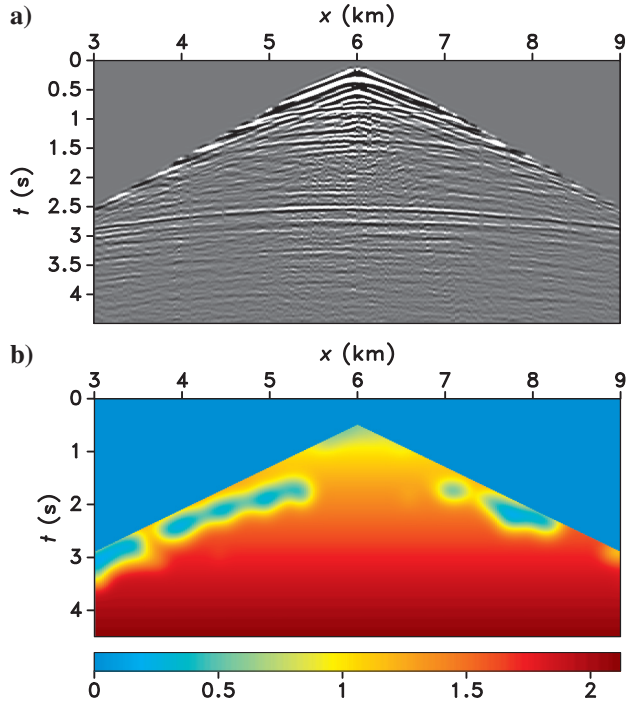


Figure 12. Volve data example. (a) One PP shot gather at $x = 6$ km, which is assumed to be a vertical displacement gather. (b) Weighting matrix for this shot gather. The weighting function mutes the direct arrivals, attenuates the predicted S-waves, and boosts later reflections.

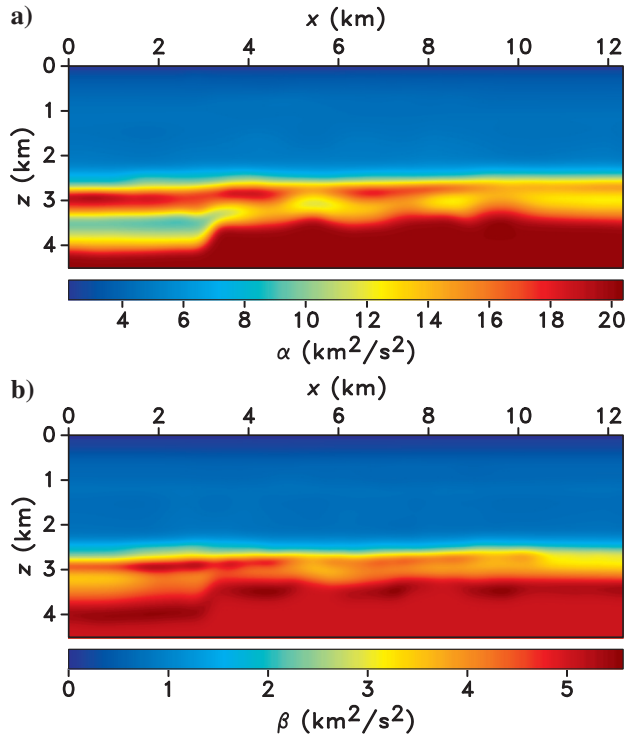


Figure 13. Volve data example. Background (a) α and (b) β models. The top water layer is from $z = 0$ to 90 m.

Downloaded 06/21/17 to 138.67.129.34. Redistribution subject to SEG license or copyright; see Terms of Use at http://library.seg.org/

Figure 18b shows mainly two types of arrivals: PP reflections with gentle slopes and converted-wave reflections with steep slopes. The amplitudes of the predicted PP reflections are relatively strong at far offset. This is to be expected because, according to Zoeppritz equation, the β model in general affects the amplitudes of PP reflections, especially at far offsets. For example, the events at $z = 2.5$–3.5 km in the $\delta\beta$ image compensate for the amplitudes of PP reflections at $z = 2.5$–3.0 s to match the observed data at far offsets.

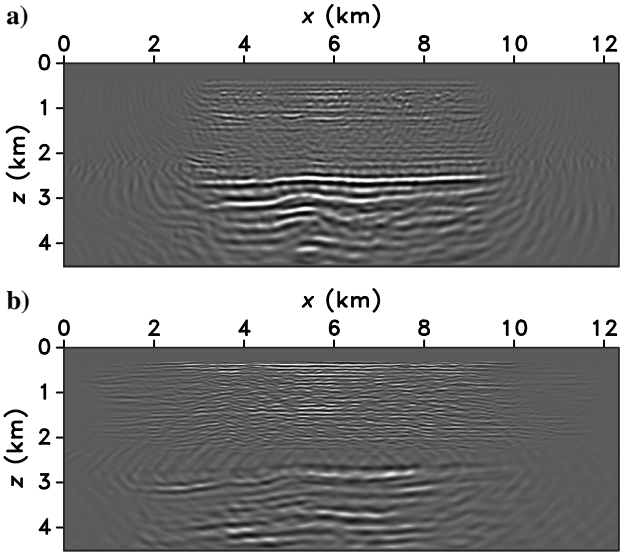


Figure 14. Volve data example. (a) The $\delta\alpha$ and (b) $\delta\beta$ RTM images. The chalk layer is from $z = 2.5$ to 3.0 km. Note that the events above the chalk layer in the $\delta\beta$ are weak and discontinuous.

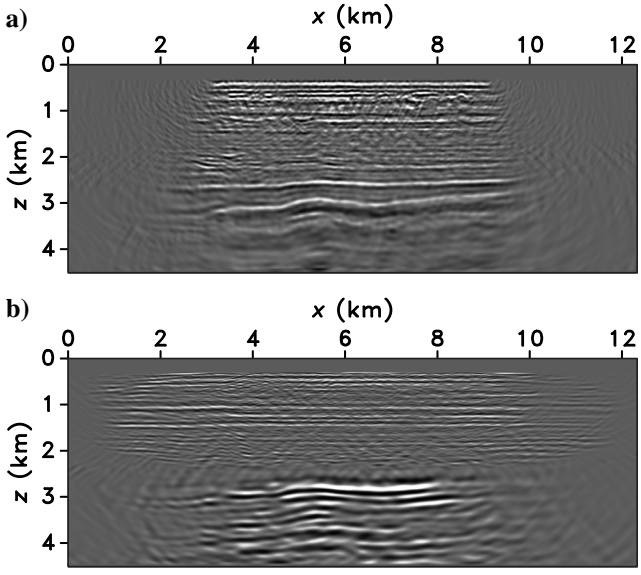


Figure 15. Volve data example. (a) The $\delta\alpha$ and (b) $\delta\beta$ LSRTM images after 12 iterations. Compared with the RTM images (Figure 14a and 14b), the LSRTM images have higher resolution and better balanced amplitudes. The reflectors at greater than 1.5 km appear in the $\delta\beta$ image after inversion with larger lateral extent along the x-direction than those in the $\delta\alpha$ image.

Figure 19 shows enlarged views of data from within the dashed box in Figure 17a: Figure 19a shows the observed data, Figure 19c shows data predicted using the $\delta\alpha$ and $\delta\beta$ images, Figure 19b shows data predicted using only the $\delta\alpha$ image, and Figure 19d shows data

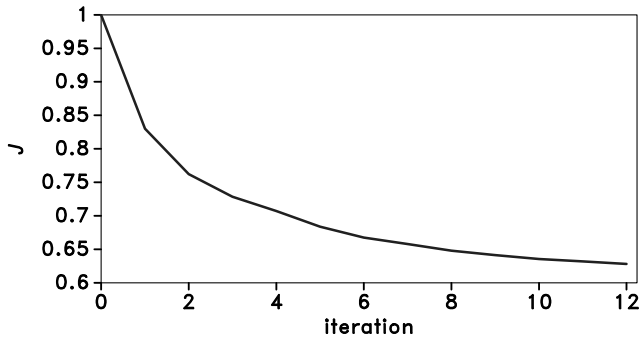


Figure 16. Volve data example. The convergence curve.

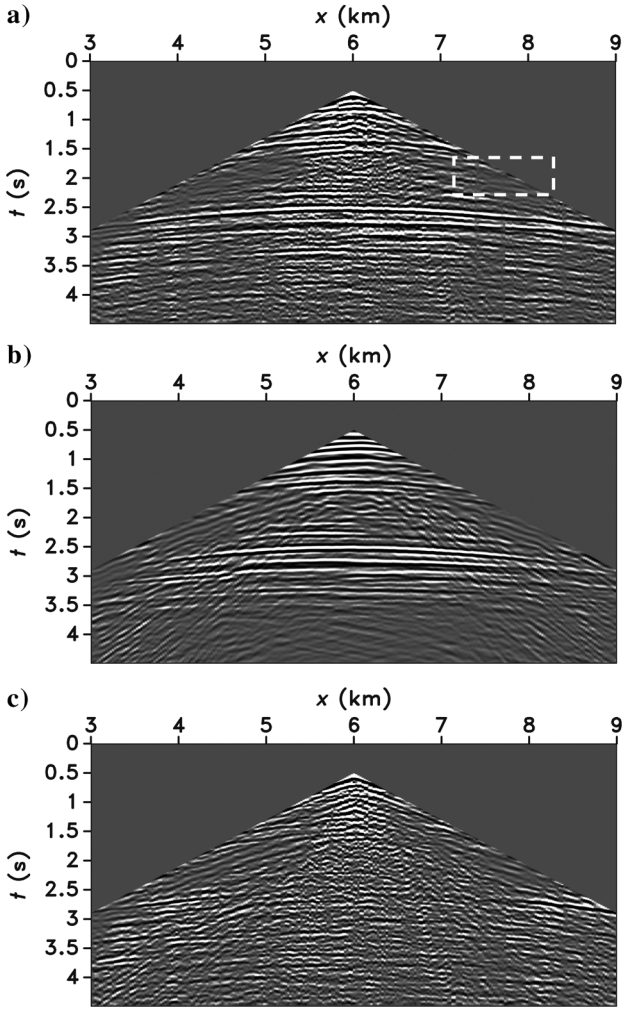


Figure 17. Volve data example. The weighted (a) observed data, (b) predicted data, and (c) data residual after 12 iterations. The predicted data accurately reproduce the dominant reflection energy seen in the observed data. The data residual contains mostly noise and some weaker reflection events.

Downloaded 06/21/17 to 138.67.129.34. Redistribution subject to SEG license or copyright; see Terms of Use at http://library.seg.org/

predicted using only the $\delta\beta$ image. The dashed line in each panel marks the same arrival, and this arrival is one that was attenuated during processed of the PP data. Notice that because the $\delta\alpha$ image predicts this arrival (shown in the bottom left panel), the $\delta\beta$ image tries to predict the same arrival but with opposite polarity (shown in the bottom right panel), so that the total prediction agrees with the observation. Had this (and other) arrivals not been removed from the observed data, we would expect the data predicted from the $\delta\alpha$ and $\delta\beta$ images, as well as the corresponding reflector amplitudes, to change accordingly. This is an illustration of how processing can negatively affect LSRTM.

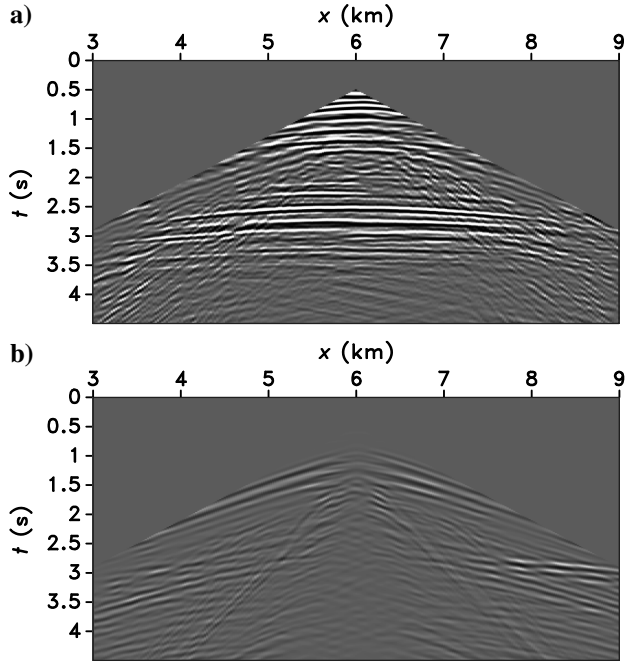


Figure 18. Volve data example. Predicted shot gathers using only (a) $\delta\alpha$ and (b) $\delta\beta$ LSRTM images. The $\delta\alpha$ image predicts most of the arrivals in the observation with correct amplitudes. The $\delta\beta$ image compensates for the amplitude variation with offset effect of the PP reflections at far offsets (e.g., $x = 8.5$ km, $t = 3.0$ s).

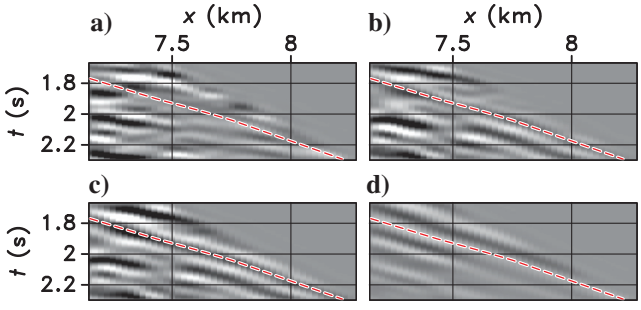


Figure 19. Volve data example. (a) Magnified views of the weighted observation, (c) prediction computed using $\delta\alpha$ and $\delta\beta$ images, (b) prediction computed using only $\delta\alpha$ image, and (d) prediction computed using only $\delta\beta$ image. A different clip from the previous plots (Figures 17a and 18b) is applied to the magnified panels for display. The box in Figure 17a indicates the magnified area. The dashed line highlights the same arrival in each panel. The $\delta\alpha$ and $\delta\beta$ images predict the same arrival with opposite polarities, so that the total prediction agrees with the observation.

We also test the inversion algorithm using PP data and PS data, which were treated as the vertical and horizontal components of the displacement vector, respectively. However, we were not able to predict both components with correct phases and amplitudes. We attribute this outcome to the fact that the data were processed for independent PP and PS imaging, and thus the arrivals in the PP and PS gathers might not be consistent with each other, in terms of phase and amplitude; therefore, this data set does not fit our elastic LSRTM algorithm underlying assumptions, which require vertical and horizontal displacement data, instead of separated PP and PS gathers.

CONCLUSION

We propose a method for elastic LSRTM using a perturbation imaging condition. The images computed using our method represent perturbations of squared P and S velocities, and they do not suffer from polarity reversals, which usually characterize conventional elastic images for converted waves. The synthetic and field data tests of the perturbation imaging condition demonstrate that elastic LSRTM produces images with fewer migration artifacts and higher resolution compared with the corresponding RTM image. The field data example also shows the importance of proper preprocessing of the recorded data, which should provide the LSRTM algorithm with data consistent with the output of the Born modeling operator.

ACKNOWLEDGMENTS

We thank the sponsors of the Center for Wave Phenomena, whose support made this research possible. We also thank Statoil ASA and the Volve license partners ExxonMobil E&P Norway AS and Bayerngas Norge AS, for the release of the Volve data. The views expressed in this paper are the views of the authors and do not necessarily reflect the views of Statoil ASA and the Volve field license partners. The reproducible numeric examples in this paper use the Madagascar open-source software package (Fomel et al., 2013) freely available from http://www.ahay.org.

REFERENCES

Artman, B., I. Podladtchikov, and A. Goertz, 2009, Elastic time-reverse modeling imaging conditions: 79th Annual International Meeting, SEG, Expanded Abstracts, 1207–1211.

Claerbout, J. F., 1992, Earth soundings analysis: Processing versus inversion: Blackwell Scientific Publications.

Claerbout, J., 2014, Geophysical image estimation by example, www. lulu .com, ISBN 978-1-312-47467-3.

Dai, W., and G. T. Schuster, 2013, Plane-wave least-squares reverse-time migration: Geophysics, **78**, no. 4, S165–S177, doi: 10.1190/geo2012-0377.1.

Dai, W., X. Wang, and G. T. Schuster, 2011, Least-squares migration of multisource data with a deblurring filter: Geophysics, **76**, no. 5, R135–R146, doi: 10.1190/geo2010-0159.1.

Denli, H., and L. Huang, 2008, Elastic-wave reverse-time migration with a wavefield-separation imaging condition: 78th Annual International Meeting, SEG, Expanded Abstracts, 2346–2350.

Dickens, T. A., and G. A. Winbow, 2011, RTM angle gathers using Poynting vectors: 81st Annual International Meeting, SEG, Expanded Abstracts, 3109–3113.

Dong, S., J. Cai, M. Guo, S. Suh, Z. Zhang, B. Wang, and Z. Li, 2012, Least-squares reverse time migration: Towards true amplitude imaging and im-

proving the resolution: 82nd Annual International Meeting, SEG, Expanded Abstracts, doi: 10.1190/segam2012-1488.1.
Du, Q., X. Gong, Y. Zhu, G. Fang, and Q. Zhang, 2012a, PS wave imaging in 3D elastic reverse-time migration: 82nd Annual International Meeting, SEG, Expanded Abstracts, doi: 10.1190/segam2012-0107.1.
Du, Q., Y. Zhu, and J. Ba, 2012b, Polarity reversal correction for elastic reverse time migration: Geophysics, **77**, no. 2, S31–S41, doi: 10.1190/geo2011-0348.1.
Duan, Y., and P. Sava, 2015, Scalar imaging condition for elastic reverse time migration: Geophysics, **80**, no. 4, S127–S136, doi: 10.1190/geo2014-0453.1.
Duan, Y., and P. Sava, 2014, Elastic reverse-time migration with OBS multiples: 84th Annual International Meeting, SEG, Expanded Abstracts, 4071–4076, doi: 10.1190/segam2014-1395.1.
Fomel, S., P. Sava, I. Vlad, Y. Liu, and V. Bashkardin, 2013, Madagascar: Open-source software project for multidimensional data analysis and reproducible computational experiments: Journal of Open Research Software, **1**, e8, doi: 10.5334/jors.ag.
Hokstad, K., R. Mittet, and M. Landrø, 1998, Elastic reverse time migration of marine walkaway vertical seismic profiling data: Geophysics, **63**, 1685–1695, doi: 10.1190/1.1444464.
Hou, J., and W. W. Symes, 2015, An approximate inverse to the extended Born modeling operator: Geophysics, **80**, no. 6, R331–R349, doi: 10.1190/geo2014-0592.1.
Huang, Y., and G. T. Schuster, 2012, Multisource least-squares migration of marine streamer and land data with frequency-division encoding: Geophysical Prospecting, **60**, 663–680, doi: 10.1111/j.1365-2478.2012.01086.x.
Hudson, J., and J. Heritage, 1981, The use of the Born approximation in seismic scattering problems: Geophysical Journal International, **66**, 221–240, doi: 10.1111/j.1365-246X.1981.tb05954.x.
Jaramillo, H. H., and N. Bleistein, 1999, The link of Kirchhoff migration and demigration to Kirchhoff and Born modeling: Geophysics, **64**, 1793–1805, doi: 10.1190/1.1444685.
Kaplan, S. T., P. S. Routh, and M. D. Sacchi, 2010, Derivation of forward and adjoint operators for least-squares shot-profile split-step migration: Geophysics, **75**, no. 6, S225–S235, doi: 10.1190/1.3506146.
Kuehl, H., and M. Sacchi, 2002, Robust AVP estimation using least-squares wave-equation migration: 72nd Annual International Meeting, SEG, Expanded Abstracts, doi: 10.1190/1.1817231.
Martin, G. S., R. Wiley, and K. J. Marfurt, 2006, Marmousi2: An elastic upgrade for Marmousi: The Leading Edge, **25**, 156–166, doi: 10.1190/1.2172306.
Nemeth, T., C. Wu, and G. T. Schuster, 1999, Least-squares migration of incomplete reflection data: Geophysics, **64**, 208–221, doi: 10.1190/1.1444517.
Patrikeeva, N., and P. Sava, 2013, Comparison of angle decomposition methods for wave-equation migration: 83rd Annual International meeting, SEG, Expanded Abstracts, 3773–3778.
Ribodetti, A., S. Operto, W. Agudelo, J.-Y. Collot, and J. Virieux, 2011, Joint ray + Born least-squares migration and simulated annealing optimization for target-oriented quantitative seismic imaging: Geophysics, **76**, no. 2, R23–R42, doi: 10.1190/1.3554330.
Rocha, D., N. Tanushev, and P. Sava, 2016, Isotropic elastic wavefield imaging using the energy norm: Geophysics, **81**, no. 4, S207–S219, doi: 10.1190/geo2015-0487.1.
Schuster, G. T., 1993, Least-squares cross-well migration: 63rd Annual International Meeting, SEG, Expanded Abstracts, 110–113.
Stanton, A., and M. Sacchi, 2015, Least squares wave equation migration of elastic data: 77th Annual International Conference and Exhibition, EAGE, Extended Abstracts, N116.
Sun, R., and G. A. McMechan, 1986, Pre-stack reverse-time migration for elastic waves with application to synthetic offset vertical seismic profiles: Proceedings of the IEEE, **74**, 457–465, doi: 10.1109/PROC.1986.13486.
Sun, R., G. A. McMechan, C. Lee, J. Chow, and C. Chen, 2006, Prestack scalar reverse-time depth migration of 3D elastic seismic data: Geophysics, **71**, no. 5, S199–S207, doi: 10.1190/1.2227519.
Szydlik, T., P. Smith, S. Way, L. Aamodt, and C. Friedrich, 2007, 3D PP/PS prestack depth migration on the Volve field: First Break, **25**, 43–47.
Trad, D., 2015, Least squares Kirchhoff depth migration: Implementation, challenges, and opportunities: 85th Annual International Meeting, SEG, Expanded Abstracts, 4238–4242, doi: 10.1190/segam2015-5833655.1.
Wong, M., B. L. Biondi, and S. Ronen, 2015, Imaging with primaries and free-surface multiples by joint least-squares reverse time migration: Geophysics, **80**, no. 6, S223–S235, doi: 10.1190/geo2015-0093.1.
Wu, R., R. Yan, X. Xie, and D. Walraven, 2010, Elastic converted-wave path migration for subsalt imaging: 80th Annual International Meeting, SEG, Expanded Abstracts, 3176–3180.
Yan, J., and P. Sava, 2008, Isotropic angle-domain elastic reverse-time migration: Geophysics, **73**, no. 6, S229–S239, doi: 10.1190/1.2981241.

Downloaded 06/21/17 to 138.67.129.34. Redistribution subject to SEG license or copyright; see Terms of Use at http://library.seg.org/